Proceedings World Geothermal Congress 2026
Calgary, Canada, June 8 – 11, 2026

Enhancing field SWIR spectroscopy analyses with laboratory calibration for quantifying clay minerals distribution in geothermal reservoirs: Lower Triassic Buntsandstein Group, Upper Rhine Graben, NE France.

Salmon M.[12]*, Glaas C.[2], Baron F.[1], Bozetti G.[3] and Patrier P.[1]

University of Poitiers, CNRS UMR 7285 IC2MP, HydrASA, Bat B8 rue Albert Turpain, TSA51106, F-86073 Poitiers Cedex 9, France [1], ES-Géothermie, 26 boulevard du Président Wilson, 67000 Strasbourg France [2], University of Strasbourg, CNRS ITES UMR 7063, 5 rue René Descartes, 67084 Strasbourg, France [3]

*manaarii.salmon@univ-poitiers.fr

Keywords: deep geothermal, hydrothermal alteration, dioctahedral clay minerals, XRD-SEM calibration.

1 INTRODUCTION

The development of geothermal energy projects in France aligns with national efforts to promote renewable energy expansion. Geothermal energy stands out as a strategic solution for supporting district heating systems as demonstrated in the Paris Basin since the 1970s (Bouniol and Maget, 1983; Laplaige et al., 2005) and for electricity production, notably in the Upper Rhine Graben (URG) since the 1980s (Baillieux et al., 2013; Genter, 1990).

Variations in thermal gradients have been observed in the URG, particularly within the fractured granitic basement and the overlying Triassic sedimentary formations, interpreted as fluid circulation in natural fractures and porosity (Baujard et al., 2017; Gérard and Kappelmeyer, 1987; Schellschmidt and Schultz, 1988). Fractures are associated to clay minerals that offer a valuable opportunity to trace hydrothermal circulation pathways, serving as sensitive indicators of geothermal brine-rock interactions (Genter et al., 2010; Glaas, 2021) using Short-Wave InfraRed (SWIR) spectroscopy (Glaas et al., 2019; Simpson and Rae, 2018; Vidal et al., 2018; Yang et al., 2001). In the Lower Triassic Buntsandstein Group (Gr.), clay minerals signature has been impacted by complex sedimentary (diagenesis) and hydrothermal histories, complicating the use of clay minerals as hydrothermal circulation tracer.

This study aims (1) to differentiate hydrothermal alteration signatures in fractured domains from diagenetic trends across the Buntsandstein units using GRT-1 and GRT-2, and (2) to develop a quantitative clay-mineral assessment by calibrating field-based SWIR spectra with laboratory XRD (Rietveld) analyses.

2 GEOLOGICAL CONTEXT

2.1 Buntsandstein

The Buntsandstein Gr. forms the basal Permian-Triassic succession at the southwestern margin of the Germanic Basin, part of the Central European Basin System (CEBS), a set of post-Variscan intracratonic basins extending from the North Sea to Central Europe (Durand and Lepper, 2013; Mader, 1985; Mansouri and Hinderer, 2021; Scheck-Wenderoth and Lamarche, 2005). Similar continental successions across western Europe highlight its regional extent (Bourquin et al., 2006). In the URG, it non-conformably overlies the Paleozoic basement and comprises a Permian Lower Buntsandstein of fluvial to aeolian sandstones and a Triassic Middle-Upper Buntsandstein, in which the Induan is missing despite an abrupt facies shift (Figure 1.A)) (Bourquin et al., 2009, 2007).

The Buntsandstein consists mainly of feldspathic to quartz-rich sandstones with subordinate siltstones and claystones deposited in semi-arid fluvial systems, with heterogeneity controlled by climatic variations and structural compartmentalization (Bourquin et al., 2009). At Rittershoffen, approximately 400 m thick succession (Figure 1.B)) includes: coarse fluvial-aeolian sandstones in the Lower Buntsandstein with (Grès anté-Annweiler (GaA) and Grès d'Annweiler (GA)); thick quartzose fluvial sand bodies in the Middle Buntsandstein (Grès Vosgiens itself separated into 3 formations Trifels (GVT), Karstahl (GVK) and Rehberg (GVR) and Conglomérat Principal (CP)) composed of laterally extensive fluvial sand bodies; and finer-grained sandstones, siltstones and claystones with local sulfate-carbonate horizons in the Upper Buntsandstein (Duringer et al., 2019).

Basin-scale subsidence and salt-related deformation further shaped sediment distribution (Maystrenko et al., 2012). The distribution of sedimentary facies, combined with varying degrees of diagenetic maturity and later hydrothermal circulation, has significantly modified porosity and mineralogy. (Bofill et al., 2024; Busch et al., 2025; Haffen et al., 2015). Regional thermal anomalies are driven by hydrothermal convection rising from the

fractured granitic basement into the Buntsandstein and Muschelkalk formations (Baillieux et al., 2013). Consequently, the Buntsandstein constitutes both a sensitive archive of fluid-rock interactions and a key geothermal reservoir in the URG.

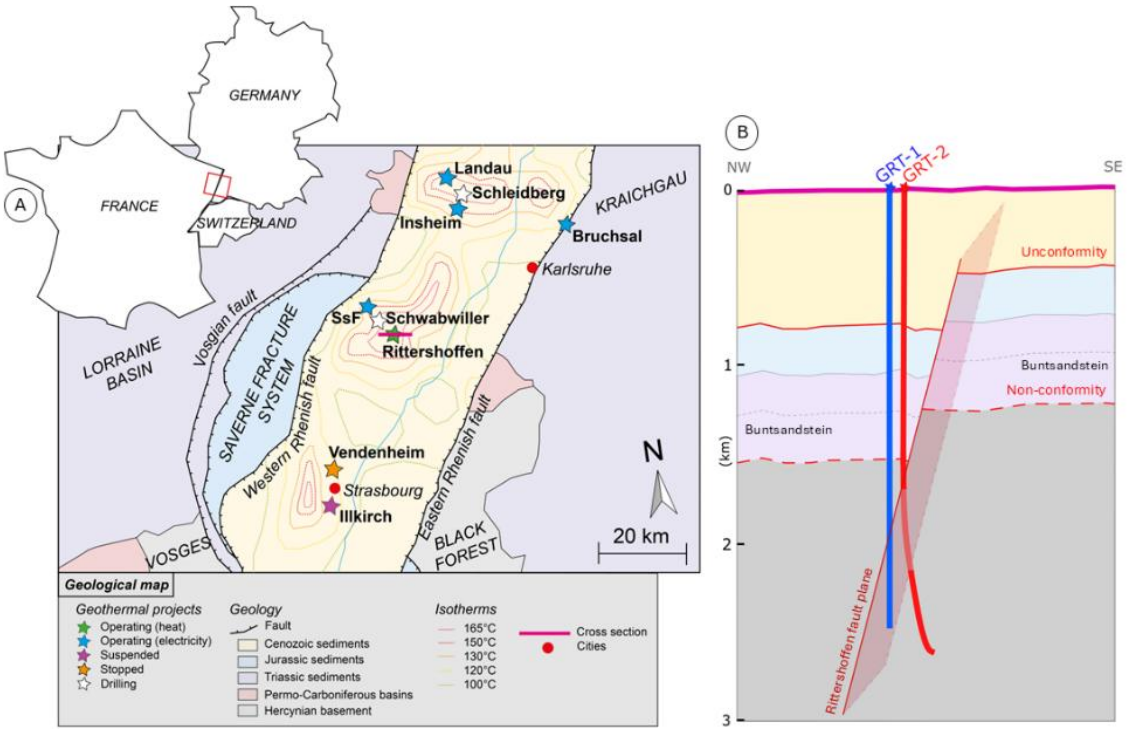


Figure 1. A) Geological map from (Glaas, 2021) based on (Baillieux et al., 2013; GeORG, 2013; Vidal et al., 2019). B) Cross-section focused on the Rittershoffen geothermal site adapted from (Glaas, 2021) .

2.2 GRT-1 and GRT-wells

The GRT-1 well, drilled in 2012 at Rittershoffen, intersects the Buntsandstein at almost 1800 m True Vertical Depth (TVD) and the granitic basement at 2200 m TVD (Figure 1.B)). It initially exhibited a low productivity index (PI) (PI < 0.5 L/s/bar), with two major permeable zones in the Muschelkalk limestone and one in the granite, all three associated with fracture networks (Baujard et al., 2017; Vidal et al., 2017). A well development strategy combining thermal, chemical, and hydraulic stimulation increased its PI to 2.5 L/s/bar (Baujard et al., 2017).

The GRT-2 well, drilled in 2014 with a 30° deviated trajectory toward the Rittershoffen Fault, reaches the Buntsandstein at 1795 m TVD and the basement at 2155 m TVD (Figure 1.B)). This demonstrates high productivity (PI = 4 L/s/bar) (Baujard et al., 2017) and intersects one major permeable zone in the Muschelkalk, one in the Buntsandstein and 4 in the granite (Baujard et al., 2017; Vidal et al., 2017).

Because GRT-2 tangentially follows the fault, its granite section shows strong hydrothermal alteration and higher fracture density over a wider interval, whereas GRT-1, crossing the fault more vertically, records a similar but more localized pattern.

3 METHODS

3.1 Buntsandstein samples

Analyses were conducted on drill cuttings from the GRT-1 and GRT-2 wells. Cutting samples were collected at 3-meter depth intervals, washed using sieves, and subsequently dried on-site at 80°C for 40 minutes.

3.2 XRD analysis

X-Ray Diffraction (XRD) analyses were performed on a Bruker D8 Advance diffractometer (CuKα radiation, 40 kV, 40 mA) in Bragg-Brentano geometry. Whole-rock powders were scanned from 3° to 75°2θ (0.015° step, 1 s/step), and mineral abundances were quantified by full-pattern Rietveld refinement using BGMN/PROFEX (Doebelin and Kleeberg, 2015). Clay mineralogy was determined on <2 µm oriented preparations in air-dried and ethylene-glycolated states. XRD patterns were collected from 2° to 35°2θ with a 0.01° step and 1 s/step. These preliminary XRD results will be refined with upcoming SEM mineral quantification to ensure accurate phase identification and proportions.

3.3 SWIR analysis

SWIR spectroscopy was performed using a field TerraSpec 4 spectrometer (Malvern Panalytical), equipped with a Si photodiode array (350-1000 nm) and two InGaAs-based scanning monochromators (1000-2500 nm), providing a spectral resolution of 3 nm in the VNIR and 10 nm in the SWIR. Measurements were acquired in reflectance mode with a contact probe and calibrated against a Spectralon® white reference. For each homogenized cutting sample, four spectra were collected, each consisting of almost 200 stacked scans to improve signal quality.

Data interpretation focused on the 1800-2500 nm interval, corresponding to OH combination bands (v+δ), including Al_2-OH near 2200 nm (dioctahedral clays), Al-Fe/Mg-OH around 2250 nm (mixed-layer or Fe/Mg-rich phases), and carbonate or Fe (II)-Mg-OH absorptions at 2330-2350 nm. Spectral deconvolution provided peak areas used as semi-quantitative mineral proxies: the 2200 nm peak for dioctahedral clays, mainly illite (Glaas et al., 2019; Vidal et al., 2018), and the 2300-2350 nm domain for carbonates and trioctahedral clays (Lypaczewski and Rivard, 2018; Madejová et al., 2017; Yang et al., 2024). Variations in the 2200 nm peak area therefore track changes in dioctahedral phyllosilicates, key markers of hydrothermal alteration along fracture corridors.

4 PRELIMINARY RESULTS AND INTERPRETATION

4.1 MINERALOGICAL CHARACTERIZATION OF BUNTSANDSTEIN IN GRT-1

The preliminary results show that dioctahedral minerals, quartz and carbonates reach almost 6 to 5%, 72 to 83% and 2 to 0% respectively from GA to the base of GVR (2158 to 2056 m) (Table 2.). This interval is characterized by relatively constant mineral proportions. A shift in this trend appears at the transition of GVR and GVK (1993 to 1948 m), where dioctahedral clay contents decrease from 3 to 2% (Table 2.). The sample at 1993 m also shows a marked enrichment in sulfates with 6% and carbonates (with almost 18%), together with a lower quartz proportion (66%) (Table 2.). This level (1993 m) therefore represents a clear mineralogical contrast within the succession.

From the base of the GVK to GaV (1948 to 1810 m), the contents of carbonates, dioctahedral and trioctahedral minerals increase from 9 to 22%, 5 to 33% and, 1 to 16%, respectively, while quartz and feldspar proportions decrease from 74 to 23% and 11 to 5% respectively (Table 2.). This trend indicates a reduction in silification and the concomitant development of secondary minerals such as clay and carbonates.

Overall, these preliminary results suggest a relatively uniform mineral composition from GA to the top of MGV, with a distinct sulfate-enriched layer at 1993 m. Above this horizon and up to the GaV, mineralogy follows a progressive evolution characterized by decreasing quartz and feldspar contents and increasing clay and carbonates abundances.

Lithology	Depth (m)	Mass percentage (%)									TOTAL
		Qz	Cb	Dioctahedral clays (Ms, Kln,...)	Trioctahedral clays (Chl, Bt, Plg)	Fds	Sul	Hem	Py	Px	
Grès à Voltzia (GaV)	1810	23	22	33	16	5	0	0	1	0	100
Couches Intermediaires (CI)	1822	41	20	16	7	9	2	1	0	4	100
Grès Vosgiens	1930	74	9	5	1	6	5	0	0	0	99
Karlstal (GVK)	1948	84	2	2	0	11	1	0	0	0	100
Grès Vosgiens	1993	66	18	3	0	7	6	0	0	0	100
Rehberg (GVR)	2056	83	0	6	0	11	0	0	0	0	100
Grès Vosgiens	2095	78	0	5	0	11	0	0	0	1	96
Trifels (GVT)	2131	82	0	5	1	8	0	0	0	1	96
Grès d'Annweiler (GA)	2158	72	2	6	0	19	0	0	0	1	100
Reddish granite	2212	62	6	8	4	20	0	0	0	0	100

Table 2. Summary table of preliminary quantitative mineral proportions from the GRT-1 well. Qz: quartz; Cb: carbonate; Ms: muscovite; Kln: kaolinite; Chl: chlorite; Bt: biotite; Plg: palygorskite; Fds: feldspar; Sul: sulfate; Hem: hematite; Py: pyrite; Px: Pyroxen.

4.2 SWIR SIGNATURES IN GRT-1 AND GRT-2

Firstly, the overall SWIR trends of GRT-1 and GRT-2 differ from the base of GaA to the top of MGV (Figure 3.). At the transition between the MGV and the UGV (around 1990 to 1970 m), both wells then follow a common trend up to the top of the GaV.

In the lower part of the section, from the base of the GaA to the unconformity between the GA and the LGV, GRT-1 and GRT-2 display similar SWIR trends and both record the same fracture zone at the GaA-GA transition (Figure

3.). this is followed, in both wells, by a pronounced SWIR peak (with amplitudes up to almost 1.5 ua) at the GA-LGV unconformity (Figure 3.). However, the semi-quantitative dioctahedral mineral proportions are consistently higher in GRT-2 by almost 2 to 3 ua compared to GRT-1 (Figure 3.). These higher values in GRT-2 correlate with its higher thermal gradient relative to GRT-1 (Glaas et al., 2025). Based on their similar SWIR trends but higher amplitudes in GRT-2, the SWIR signal suggests the presence of a permeable Permian interval in GRT-2.

From the GA to the top of the MGV, the dioctahedral mineral proportions in GRT-1 remain smooth and nearly constant (Figure 3.). In contrast, the SWIR responses in GRT-2 are highly variable, reflecting an interval affected by alternating mineralogical assemblages including dioctahedral clays and secondary minerals such as quartz, barite, or carbonates. This structure sugggests the presence of zones enriched in dioctahedral minerals (e.g., illitic phases) alternating with zones potentially sealed by secondary minerals precipitation. The upper limit of this first characteristic interval is marked by a strong SWIR peak in both wells, reaching 7 ua, associated with a major fracture zone (Figure 3.). at this depth, GRT-1 and GRT-2 intersect a geological layer with similar dioctahedral mineral proportions, suggesting comparable petrophysical characteristics. However, only GRT-2 exhibits a thermal anomaly of almost +1.6°C (Glaas et al., 2025). While both wells cross the same geological layer, only GRT-2 seems to record a permeable zone, implying an increase in dioctahedral minerals within a damage zone located above this fracture zone and extending to the base of the MGV.

The second main SWIR trend, from the transition between the MGV and UGV up to the top of the GaV, shows similar behaviour in both wells (Figure 3.). Dioctahedral mineral proportions reach 5 to 6 ua up to the UGV-CI unconformity, then increase further to almost 8 ua in both wells (Figure 3.). However, GRT-1 shows a marked depletion in dioctahedral minerals between 1930 and 1910 m, suggesting enrichment in non-hydroxylated secondary minerals (e.g., quartz, barite or others). These minerals likely sealed porosity in this interval, as no thermal anomaly is observed (Glaas et al., 2025).

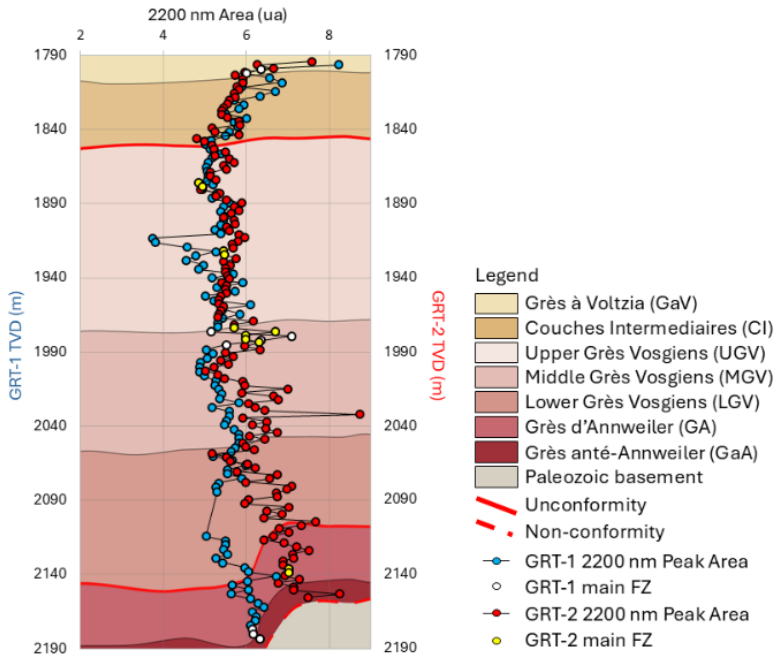


Figure 3. Evolution of SWIR semi-quantitative proportion of di-octahedral mineral in GRT-1 and GRT-2.

5 CONCLUSION

Taken together, the SWIR and XRD datasets outline a coherent mineralogical and spectral evolution through the Buntsandstein Gr. while revealing strong contrasts between GRT-1 and GRT-2. In GRT-1, XRD results show a transition from quartz-rich sandstones at the base to increasingly clay- and carbonate-rich intervals toward the GaV, including a distinct sulfate-enriched horizon at 1993 m (Table 2.). SWIR profiles validate this trend, displaying a smooth and homogeneous 2200 nm signal consistent with a poorly permeable matrix. In contrast, GRT-2 exhibits highly variable spectral and mineralogical signatures, with alternating illite-rich intervals and zones sealed by secondary minerals (Figure 3). These fluctuations, together with the thermal anomaly observed in GRT-2, indicate localized hydrothermal alteration and enhanced permeability within a structurally connected damage zone, despite both wells intersecting comparable stratigraphic levels (Glaas et al., 2025). Together, these results underline the value of combining SWIR and XRD to resolve reservoir heterogeneity. Ongoing work includes quantitative mineralogy (Rietveld refinement) and SEM-based clay polytype analysis to distinguish

diagenetic (2M1, 1Md) from hydrothermal (1M, fibrous) illite, refine mineralogical attribution of SWIR indices, and better constrain fracture pathways and permeability distribution within Buntsandstein.

Acknowledgements

This work was carried out within the FindHeat project (EU Grant Agreement No. 101147171). It was supported by a French government grant managed by the Agence Nationale de la Recherche under the France 2030 initiative (ANR-22-EXSS-0010) and by the France 2030 program through EUR INTREE (ANR-18-EURE-0010). The authors acknowledge financial support from the European Regional Development Fund (ERDF) and the Région Nouvelle-Aquitaine, as well as support from the PEPR Fossé Rhénan project. We thank ECOGI for providing access to the Rittershoffen dataset. Part of the results presented here were obtained on the "environmental mineralogy" platform at IC2MP. The views expressed are those of the authors and do not necessarily reflect those of the European Union or CINEA.

REFERENCES

Baillieux, P., Schill, E., Edel, J.-B., Mauri, G., 2013. Localization of temperature anomalies in the Upper Rhine Graben: insights from geophysics and neotectonic activity. Int. Geol. Rev. 55, 1744–1762. https://doi.org/10.1080/00206814.2013.794914

Baujard, C., Genter, A., Dalmais, E., Maurer, V., Hehn, R., Rosillette, R., Vidal, J., Schmittbuhl, J., 2017. Hydrothermal characterization of wells GRT-1 and GRT-2 in Rittershoffen, France: Implications on the understanding of natural flow systems in the rhine graben. Geothermics 65, 255–268. https://doi.org/10.1016/j.geothermics.2016.11.001

Bofill, L., Bozetti, G., Schäfer, G., Ghienne, J.-F., Schuster, M., Scherer, C., De Souza, E., 2024. Quantitative facies analysis of a fluvio-aeolian system: Lower Triassic Buntsandstein Group, eastern France. Sediment. Geol. 465, 106634. https://doi.org/10.1016/j.sedgeo.2024.106634

Bouniol, B., Maget, P., 1983. Ressources geothermiques au lusitanien dans le bassin parisien (no. 83 sgn 0445 gth). bureau de recherches geologiques et minières.

Bourquin, S., Durand, M., Diez, J.B., Broutin, J., Fluteau, F., 2007. The Permian-Triassic boundary and lower Triassic sedimentation in western European basins: an overview.

Bourquin, S., Guillocheau, F., Péron, S., 2009. Braided rivers within an arid alluvial plain (example from the Lower Triassic, western German Basin): recognition criteria and expression of stratigraphic cycles. Sedimentology 56, 2235–2264. https://doi.org/10.1111/j.1365-3091.2009.01078.x

Bourquin, S., Peron, S., Durand, M., 2006. Lower Triassic sequence stratigraphy of the western part of the Germanic Basin (west of Black Forest): Fluvial system evolution through time and space. Sediment. Geol. 186, 187–211. https://doi.org/10.1016/j.sedgeo.2005.11.018

Busch, B., Böke, L.L., Schmidt, C., Warnecke, M., Hilgers, C., 2025. Reservoir quality controls in the Lower Buntsandstein and their relation to detrital grain size, URG, SW-Germany. Geothermics 132, 103453. https://doi.org/10.1016/j.geothermics.2025.103453

Doebelin, N., Kleeberg, R., 2015. Profex: a graphical user interface for the Rietveld refinement program BGMN. J. Appl. Crystallogr. 48, 1573–1580.

Durand, M., Lepper, Ü.J., 2013. 9.4 Der Buntsandstein in Nordost-Frankreich.

Duringer, P., Aichholzer, C., Orciani, S., Genter, A., 2019. The complete lithostratigraphic section of the geothermal wells in Rittershoffen (Upper Rhine Graben, eastern France): a key for future geothermal wells. BSGF-Earth Sci. Bull. 190, 13.

Genter, A., 1990. Géothermie roches chaudes sèches : le granite de soultz-sous-forêts (bas-rhin, france). editions du brgm.

Genter, A., Evans, K., Cuenot, N., Fritsch, D., Sanjuan, B., 2010. Contribution of the exploration of deep crystalline fractured reservoir of Soultz to the knowledge of enhanced geothermal systems (EGS). Comptes Rendus Geosci. 342, 502–516. https://doi.org/10.1016/j.crte.2010.01.006

GeORG, 2013. GeORG: Potentiel géologique profond du Fossé rhénan supérieur. Partie 1 - 4.

Gérard, A., Kappelmeyer, O., 1987. The Soultz-sous-Forêts project. Geothermics 16, 393–399.

Glaas, C., 2021. Mineralogical and structural controls on permeability of deep naturally fractured crystalline reservoirs. Insights from geothermal wells (Upper Rhine Graben).

Glaas, C., Salmon, M., Baron, F., Bozetti, G., Knobelock, G., Rumbach, G., Patrier, P., Baczkowski, C., Genter, A., 2025. Are Triassic rocks of the Upper Rhine Graben a geothermal reservoir? Insights from Rittershoffen wells with geophysical logs and SWIR spectroscopy. Presented at the European Gaothermal Congress (EGC), Zurich Switzerland.

Glaas, C., Vidal, J., Patrier, P., Girard, J.-F., Beaufort, D., Petit, S., Genter, A., 2019. How Do Secondary Minerals in Granite Help Distinguish Paleo- from Present-Day Permeable Fracture Zones? Joint Interpretation of SWIR Spectroscopy and Geophysical Logs in the Geothermal Wells of Northern Alsace. Geofluids 2019, 1–20. https://doi.org/10.1155/2019/8231816

Haffen, S., Geraud, Y., Diraison, M., 2015. Geothermal, Structural and Petrophysical Characteristics of Buntsandstein Sandstone Reservoir (Upper Rhine Graben, France).

Laplaige, P., Lemale, J., Decottegnie, S., Desplan, A., Goyeneche, O., Delobelle, G., 2005. Geothermal resources in France. Current situation and prospects.

Lypaczewski, P., Rivard, B., 2018. Estimating the Mg# and AlVI content of biotite and chlorite from shortwave infrared reflectance spectroscopy: Predictive equations and recommendations for their use. Int. J. Appl. Earth Obs. Geoinformation 68, 116–126. https://doi.org/10.1016/j.jag.2018.02.003

Madejová, J., Gates, W.P., Petit, S., 2017. IR Spectra of Clay Minerals, in: Developments in Clay Science. Elsevier, pp. 107–149. https://doi.org/10.1016/B978-0-08-100355-8.00005-9

Mader, D. (Ed.), 1985. Prologue, in: Aspects of Fluvial Sedimentation in the Lower Triassic Buntsandstein of Europe. Springer, Berlin, Heidelberg, pp. 1–12. https://doi.org/10.1007/BFb0010513

Mansouri, M., Hinderer, M., 2021. Towards a sediment budget of Permo-Triassic successions in the Central European Basin - Implications for terrestrial perturbations around the Permian-Triassic Boundary (PTB). J. Appl. Reg. Geol. Z. Dtsch. Ges. Für Geowiss. ZDGG 172, 565–590. https://doi.org/10.1127/zdgg/2020/0239

Maystrenko, Y.P., Bayer, U., Scheck-Wenderoth, M., 2012. Regional-scale structural role of Permian salt within the Central European Basin System. Geol. Soc. Lond. Spec. Publ. 363, 409–430. https://doi.org/10.1144/SP363.19

Scheck-Wenderoth, M., Lamarche, J., 2005. Crustal memory and basin evolution in the Central European Basin System—new insights from a 3D structural model. Tectonophysics 397, 143–165. https://doi.org/10.1016/j.tecto.2004.10.007

Schellschmidt, R., Schultz, R., 1988. Hydrogeothermic studies on Hot Dry Rock technology. (No. 105423).

Simpson, M.P., Rae, A.J., 2018. Short-wave infrared (SWIR) reflectance spectrometric characterisation of clays from geothermal systems of the Taupō Volcanic Zone, New Zealand. Geothermics 73, 74–90. https://doi.org/10.1016/j.geothermics.2018.01.006

Vidal, J., Genter, A., Chopin, F., 2017. Permeable fracture zones in the hard rocks of the geothermal reservoir at Rittershoffen, France. J. Geophys. Res. Solid Earth 122, 4864–4887. https://doi.org/10.1002/2017JB014331

Vidal, J., Glaas, C., Hébert, B., Patrier, P., Beaufort, D., Genter, A., 2018. Use of SWIR spectroscopy for the exploration of permeable fracture zones in geothermal wells at Rittershoffen (Alsace, France). Geotherm. Resour. Counc. Reno USA 10.

Vidal, J., Hehn, R., Glaas, C., Genter, A., 2019. How Can Temperature Logs Help Identify Permeable Fractures and Define a Conceptual Model of Fluid Circulation? An Example from Deep Geothermal Wells in the Upper Rhine Graben. Geofluids 2019, 1–14. https://doi.org/10.1155/2019/3978364

Yang, K., Browne, P.R.L., Huntington, J.F., Walshe, J.L., 2001. Characterising the hydrothermal alteration of the Broadlands–Ohaaki geothermal system, New Zealand, using short-wave infrared spectroscopy. J. Volcanol. Geotherm. Res. 106, 53–65. https://doi.org/10.1016/S0377-0273(00)00264-X

Yang, Y., Meng, L., Zhang, J., Gao, Y., Hao, Z., Liu, Y., Niu, M., Zhang, X., Liu, X., Liu, S., 2024. Near-Infrared Light-Driven MXene/Liquid Crystal Elastomer Bimorph Membranes for Closed-Loop Controlled Self-Sensing Bionic Robots. Adv. Sci. 11. https://doi.org/10.1002/advs.202307862